Photodissociation cross sections and rates of NaO

Tianrui Bai,[1,2] Xinglin Yang,[1] Zhi Qin ®[2,3]★ and Linhua Liu ®[2,3,4]★

[1]*School of Energy and Power, Jiangsu University of Science and Technology, Zhenjiang, 212100 Jiangsu, China*

[2]*School of Energy and Power Engineering, Shandong University, Jinan, 250061 Shandong, China*

[3]*Optics and Thermal Radiation Research Center, Institute of Frontier and Interdisciplinary Science, Shandong University, Qingdao, 266237 Shandong, China*

[4]*School of Energy Science and Engineering, Harbin Institute of Technology, Harbin, 150001 Heilongjiang, China*

ABSTRACT

Photodissociation of NaO may be important for the sodium chemistry in various astrophysical regions. This work produces the photodissociation cross sections and rates of NaO over the temperature range from 0 to 15 000 K. First, the state-resolved cross sections for transitions from the ground and first excited states of NaO are investigated using *ab initio* potential energy curves and transition dipole moments. The temperature-dependent cross sections were then obtained by assuming a Boltzmann distribution to describe the population of the initial state. Detailed comparisons with experimental cross sections at 200 and 300 K reveal that the $X\,^2\Pi \to 1\,^2\Delta$ and $X\,^2\Pi \to 2\,^2\Sigma^-$ transitions may be the main photodissociation pathways for NaO in the wavelengths of about 2400–2580 Å, while the $X\,^2\Pi \to B\,^2\Sigma^-$ transition may play a dominant role in the wavelengths of about 3534–4230 Å. Finally, photodissociation rates in the interstellar, solar, and blackbody radiation fields were determined. In the interstellar and solar radiation fields, the $X\,^2\Pi \to B\,^2\Sigma^-$ transition dominates at low temperatures and the $A\,^2\Sigma^+ \to 2\,^2\Sigma^+$ transition dominates at high temperatures. The total photodissociation rates in ultraviolet-rich and visible-rich radiation fields are almost insensitive to the temperature. The photodissociation cross sections and rates of NaO should be useful for investigating the chemical evolution of the sodium element in planetary exospheres, atmospheres of cool stars, and envelopes of evolved stars.

Key words: astrochemistry – molecular data – molecular processes.

1. INTRODUCTION

The atomic sodium (Na) layer occurs globally from about 80 to 100–110 km in the upper mesosphere, and the concentration of the Na atom reaches a peak of several thousand atoms per cubic centimetre near 90 km (Plane 1991). It is generally accepted that the meteoric ablation is responsible for the formation of the Na layer, because the meteoric material entering into the Earth's atmosphere is estimated to be about 44 tons per day and ablates at altitudes between 80 and 90 km (Hugthes 1978). The atomic Na, as the most readily observed species, has also been detected on other planets in the solar system. For example, Na was observed around Europa and Io, the satellites of Jupiter (Brown & Hill 1996; Mendillo et al. 2007). Due to the bright emission line of Na, it also served as an excellent proxy to investigate the process governing the composition of the lunar and Mercury's exosphere (Potter & Morgan 1988; McClintock & Lankton 2007; Sprague et al. 2012). Additionally, a bright Na spot was also detected in the lunar orbit after maximum of Leonid 1998 meteor shower (Smith et al. 1999).

Photodissociation is thought to be a source of the Na atoms in planetary exospheres (Valiev et al. 2020). According to studies of the volcanic outgassing in Io's atmosphere, the predominant production mechanism for Na is believed to be the photolysis of NaCl released from volcanic activity (Moses et al. 2002). As a constituent in the lunar exosphere, Na is also thought to be generally produced by the photo-stimulated desorption in the equator (Hunten & Sprague 1997; Yakshinskiy & Madey 1999; Sarantos et al. 2010). In addition, the studies on the chemistry of impact events on Moon and Mercury show that NaO can be formed following the meteoroid bombardment and subsequently destroyed by solar photons due to relatively short photolysis lifetimes compared to ballistic flight times (Berezhnoy 2013; Berezhnoy 2018). In the mesosphere region, the Na layer is characterized as a photochemical-dynamical coupled system and the photolysis of NaO plays an important role in the photochemistry of the sodium layer. This is mainly due to the fact that Na atoms resulting from photodissociation retain an energy of the order of the molecular bond strength, which exist in an energetic (1–2 eV) Na population. The generated Na radicals can participate in the formation of other Na-bearing species, such as NaOH, NaO_2, $NaHCO_3$, and so on (Self & Plane 2001; Plane 2004).

Cross sections and rate coefficients are main parameters for understanding photodissociation processes and can be employed to analyse the photochemical timescale of the Na layer's chemical system and the transport behavior of Na to the exosphere (Xu & Smith 2005; Berezhnoy 2013, 2018; Valiev et al. 2017). Self and Plane (2001) measured the absolute photolysis cross sections of NaO between 193 and 423 nm at

Table 1 Dissociation limits for the molecular electronic states considered in the NaO photodissociation processes.

Electronic states	Separated-atom atomic states	Dissociation limit/cm^{-1} Exp.[a]	Our results	α_o[b]	C_6	$C_5/10^4$
X $^2\Pi$	Na $(2p^63s\ ^2S_g)$ + O $(2s^22p^4\ ^3P_g)$	0	0	6.08	203.72	54.61
B $^2\Sigma^-$				4.99	167.20	70.69
A $^2\Sigma^+$	Na $(2p^63s\ ^2S_g)$ + O $(2s^22p^4\ ^1D_g)$	15 867.86	15 876.28	4.94	165.52	162.15
C $^2\Pi$				5.19	173.90	25.98
1 $^2\Delta$				5.92	198.36	5.26
2 $^2\Sigma^-$	Na $(2p^63p\ ^2P_g)$ + O $(2s^22p^4\ ^3P_g)$	17 157.39	16 380.24	4.99	280.18	328.37
2 $^2\Sigma^+$				6.08	503.95	17.01

[a]Experimental data from NIST Atomic Spectra Database (Kramida et al. 2022).
[b]The polarizabilities from Medved et al. (2000).

200 and 300 K, subsequently deriving photolysis rates. Valiev et al. (2020) theoretically determined the photodissociation cross sections of NaO between 360 and 480 nm using quantum chemistry methods. However, the photodissociation cross sections of NaO between 91.2 and 250 nm capture more attention in the astrochemistry due to the high intensity of the interstellar radiation field (ISRF) in this wavelength range. In addition, the photodissociation cross section of NaO calculated by Valiev et al. (2020) was about 1×10^{-17} cm^2 at 420 nm, which was far larger than the experimental value of 5.22×10^{-19} cm^2 at 423 nm (Self & Plane 2001). Such a large discrepancy may be attributed to the approximations used in solving the wave functions. Therefore, this study aims to obtain more accurate photodissociation cross sections and rates of NaO by directly solving the Schrödinger equation.

The first excited state of NaO (i.e. A $^2\Sigma^+$) has a low electronic excitation energy and a long radiative lifetime and is easy to populate when the temperature rises, thus this study focuses on investigating the photodissociation processes from both the ground and first excited states. First, we calculated the potential energy curves (PECs) of seven electronic states and the transition dipole moments (TDMs) for transitions from the X $^2\Pi$ and A $^2\Sigma^+$ states using the *ab initio* methodology. Then, we investigated the state-resolved cross sections for transitions from all rovibrational levels of the X $^2\Pi$ and A $^2\Sigma^+$ states within the wavelength range of 50–5000 nm and temperature-dependent cross sections for temperatures ranging from 0 to 15 000 K. Finally, photodissociation rates in the interstellar, solar, and blackbody radiation fields were obtained and analysed.

2. THEORY AND CALCULATIONS

2.1 PECs and TDMs

In this work, we considered the photodissociation of NaO involving seven electronic states, including the X $^2\Pi$, A $^2\Sigma^+$, B $^2\Sigma^-$, C $^2\Pi$, 1 $^2\Delta$, 2 $^2\Sigma^-$, and 2 $^2\Sigma^+$ states. The PECs and TDMs were calculated using the complete active space self-consistent field method, followed by the valence internally contracted multireference configuration interaction (icMRCI) approach with the Davidson correction. These calculations were performed using the MOLPRO 2015 software package (Werner et al. 2015). To accurately represent the electronic structure of NaO, the augmented correlation-consistent polarized core-valence sextet-zeta basis set, aug-cc-pCV6Z, was used. All the computations were carried out in the C$_{2v}$ point group. The electrons in the 1s, 2s, and 2p shells of Na, as well as 1s and 2s shells of O, were put into six closed-shell orbitals. The rest of electrons in the 3s shell of Na and 2p shell of O were put into the active space.

The PECs and TDMs were calculated over the internuclear distances from 1.12 to 10 Å. To accurately determine the photodissociation cross sections and rates, the extrapolation is required for both short and long internuclear ranges. The form of the short-range potentials can be expressed by

$$V(R) = A \exp(-BR) + C \tag{1}$$

where A, B, and C are fitting parameters and can be obtained by fitting *ab initio* potential points. For the long-range forms, the PECs can be extrapolated by the following function (Chang 1967; Babb et al. 2019):

$$V(R) = -\frac{C_5}{R^5} - \frac{C_6}{R^6} + V(R \to \infty) \tag{2}$$

where C_6 is the dipole–dipole dispersion (van der Waals) coefficient and can be calculated by the London formula (London 1937)

$$C_6 = \frac{3}{2} \frac{\tau_{Na}\tau_O}{\tau_{Na} + \tau_O} \alpha_{Na}\alpha_O \tag{3}$$

where τ is the ionization energy of the atom, which can be obtained from the NIST Atomic Spectra Database (Kramida et al. 2022). α are the static dipole polarizabilities, which are 162.88 au for the ground state ^2S_g, 273 au for the excited state $^2P_g(0)$, and 403 au for the $^2P_g(\pm1)$ state of Na, respectively (Magnier & Aubert-Frécon 2002). The polarizabilities for the ground and excited states of oxygen have been calculated using the CASPT2 method (Medved et al. 2000), and the resulting values are shown in Table 1. C_5 is the quadrupole-quadrupole electrostatic

interaction and can be estimated by fitting *ab initio* points. The same extrapolations at the short and long internuclear distances were also performed for the TDMs. A cubic spline was used to interpolate the *ab initio* points.

2.2 Photodissociation cross sections

For the direct photodissociation, a brief overview for the calculation of the cross sections are given below. Detailed descriptions can refer to previous papers (Bai et al. 2021; Qin et al. 2021, 2022a,b). The state-resolved cross section for a bound-free transition from initial rovibrational level $\upsilon''N''$ can be calculated by (Kirby & Dishoeck 1989)

$$\sigma_{\upsilon''N''}\left(E_{ph}\right) = 2.689 \times 10^{-18} \times E_{ph}g \sum_{N'} \left(\frac{1}{2N''+1} S\left(N'J', N''J''\right) |\langle \chi_{k'N'}\left(R\right)|D\left(R\right)| \chi_{\upsilon''N''}\left(R\right)\rangle|^2\right) \tag{4}$$

where E_{ph} is the photon energy and g are the degeneracy factors (equal to 1 for the $\Sigma \leftrightarrow \Sigma$, $\Pi \to \Sigma$, $\Pi \to \Delta$, and $\Pi \leftrightarrow \Pi$ transitions and 2 for the $\Sigma \to \Pi$ transitions), $S(N'J', N''J'')$ are the Hönl-London factors (Kovács 1969). $D(R)$ are the TDMs. $\chi_{k'N'}(R)$ are the energy-normalized continuum wave functions and $\chi_{\upsilon''N''}(R)$ are the bound wave functions. The renormalized Numerov method (Johnson 1977, 1978) was used to solve the radial Schrödinger equation to obtain wave functions and eigenvalues. J, υ, N are the total angular, vibrational, and rotational momentum quantum numbers, respectively. The final state is denoted with a single prime superscript and the initial state with a double prime.

A Boltzmann distribution can be used to describe the population of rovibrational levels of the initial state. Thus, the photodissociation cross sections can be expressed by (Pattillo et al. 2018)

$$\sigma\left(\lambda, T_g\right) = \frac{\sum_{\upsilon''}^{\upsilon_{max}} \sum_{N''}^{N_{max}(\upsilon)} (2 - \delta_{\Lambda''})(2S+1)(2N''+1) \exp\left(-\left(E_{\upsilon''N''} - \varepsilon_0\right)/k_B T_g\right) \sigma_{\upsilon''N''}}{Q\left(T_g\right)} \tag{5}$$

where $Q(T_g)$ is the rovibrational partition function and can be expressed as (Hanson et al. 2016)

$$Q\left(T_g\right) = \sum_{n}^{n_{max}} \sum_{\upsilon}^{\upsilon_{max}(n)} \sum_{N}^{N_{max}(n,\upsilon)} (2 - \delta_{\Lambda}) (2S+1) (2N+1) \exp\left(-\left(E_{n\upsilon N} - \varepsilon_0\right)/k_B T_g\right) \tag{6}$$

where T_g is the temperature of the surrounding gas, λ is the wavelength of the incident photon. $E_{n\upsilon N}$ is the energy of the n-th electronic state with quantum numbers υ, N, and ε_0 refers to the energy of the lowest energy level. S is the spin quantum number. h, k_B and c are the Planck's constant, Boltzmann constant and the speed of light in vacuum, respectively.

2.3 Photodissociation rates

The photodissociation rate of a molecule exposed to a radiation field can be obtained by

$$k\left(T_g\right) = \int \sigma\left(\lambda, T_g\right) I\left(\lambda\right) d\lambda \tag{7}$$

where $I(\lambda)$ is the photon intensity from the radiation field summed over all incident angles. The interstellar, solar, and blackbody radiation fields were considered in this work, and the intensities of these radiation fields are shown in Fig. 1. Note that the blackbody radiation fields were normalized to match the integrated energy intensity of the ISRF between 91.2 and 200 nm, which is 2.6×10^{-6} W m^{-2}, as reported by Heays et al. (2017) .

3. RESULTS AND DISCUSSION

3.1 PECs and TDMs

The PECs of seven electronic states (X $^2\Pi$, A $^2\Sigma^+$, B $^2\Sigma^-$, C $^2\Pi$, 1 $^2\Delta$, 2 $^2\Sigma^+$, and 2 $^2\Sigma^-$) and the TDMs for eight transitions from the X $^2\Pi$ and A $^2\Sigma^+$ states were calculated, as shown in Fig. 2. It can be observed that these states correspond to three dissociation limits, namely Na (^2S_g) + O (^3P_g), Na (^2S_g) + O (^1D_g), and Na (^2P_g) + O (^3P_g). The relative energies of these dissociation limits were calculated and listed in Table 1. The calculated energy of the second dissociation limit agrees well with experimental value (Kramida et al. 2022), while our calculation underestimates the energy of the third dissociation limit. To obtain reasonable band positions in the absorption spectra, the energies of the second and third dissociation limits were adjusted to align with experimental dissociation limits for the subsequent calculations of cross sections and rates.

The spectroscopic parameters of three bound electronic states (X $^2\Pi$, A $^2\Sigma^+$, and C $^2\Pi$) were determined by fitting the vibrational levels. Table 2 lists our calculated spectroscopic parameters, along with previous experimental and theoretical results. Our calculated harmonic constant ω_e for the ground state is closer to the experimental value (Yamada et al. 1989) than the previous calculated one from Langhoff et al. (1991), but the equilibrium bond distance R_e deviates from the experimental value by 0.029 Å. For the A $^2\Sigma^+$ state, the difference of the electronic excitation energy T_e is about 314.08 cm^{-1} relative to the experiment value (Joo et al. 1999). Previous studies (Semenov et al. 2021; Bai et al. 2023) have demonstrated that the energy levels are highly sensitive to the values of T_e and R_e, thus we modify the calculated PECs of the X $^2\Pi$ and A $^2\Sigma^+$ states to match the experimental values for the subsequent calculations of photodissociation cross sections and rates.
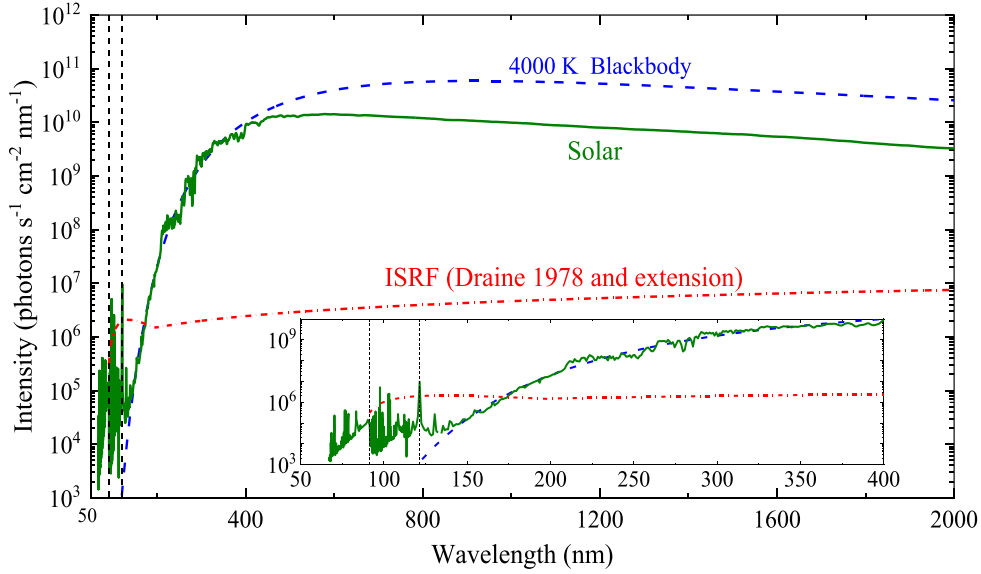
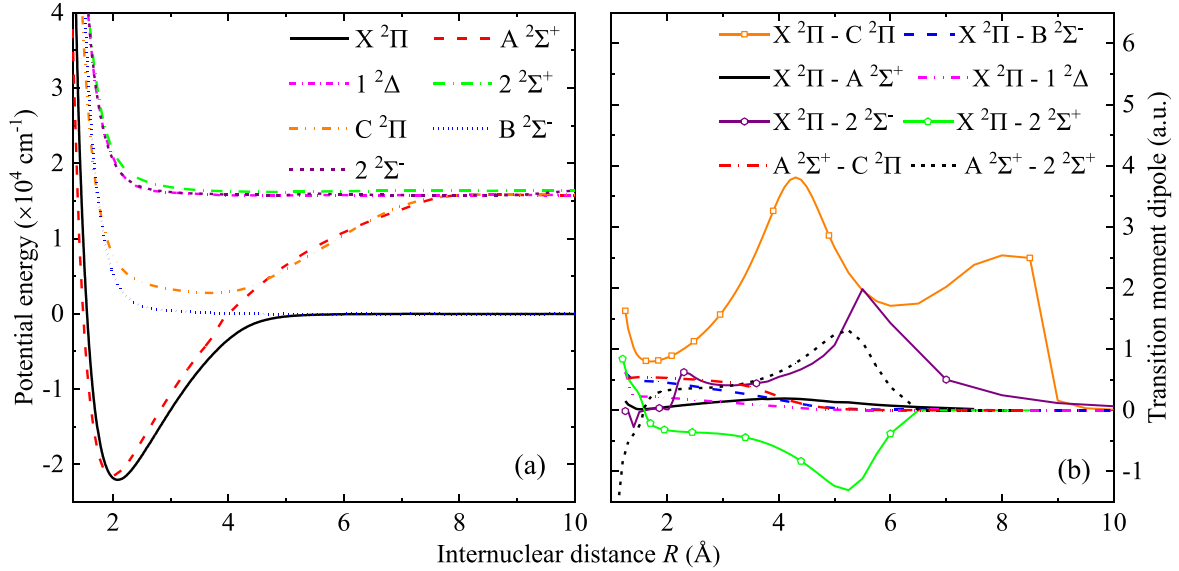**Figure 1.** Wavelength dependence of some astrophysically-relevant radiation fields.

Figure 2. *Ab initio* points of (a) the PECs of each considered electronic state of NaO and (b) the TDMs for the electronic transitions from the ground and first excited states.

Table 2 Spectroscopic parameters of three electronic states of NaO obtained by the icMRCI + Q method.

State		T_e/cm^{-1}	ω_e/cm^{-1}	$\omega_e x_e$/cm^{-1}	B_e	α_e/$\times 10^{-3}$cm^{-1}	R_e/Å
X $^2\Pi$	This work	0	475.41	1.2916	0.4125	4.06	2.081
	Exp. [a]	0	492.27		0.4243		2.052
	Cal. [b]	0	463				2.061
	Cal. [d]	0				4.3	2.054
A $^2\Sigma^+$	This work	1678.83	497.05	3.54 08	0.4536	5.15	1.990
	Exp. [c]	1992.905			0.462		
	Cal. [b]	1902	495				1.963
	Cal. [d]	1831				5.9	1.951
C $^2\Pi$	This work	24 822.58	97.28	0.3502	0.1292	3.17	3.719
	Cal. [b]	24 201	105				3.594

[a] Experiment (Yamada et al. 1989), [b] Calculation (Langhoff et al. 1991), [c] Experiment (Joo et al. 1999), [d] Calculation (Soldán et al. 1999).
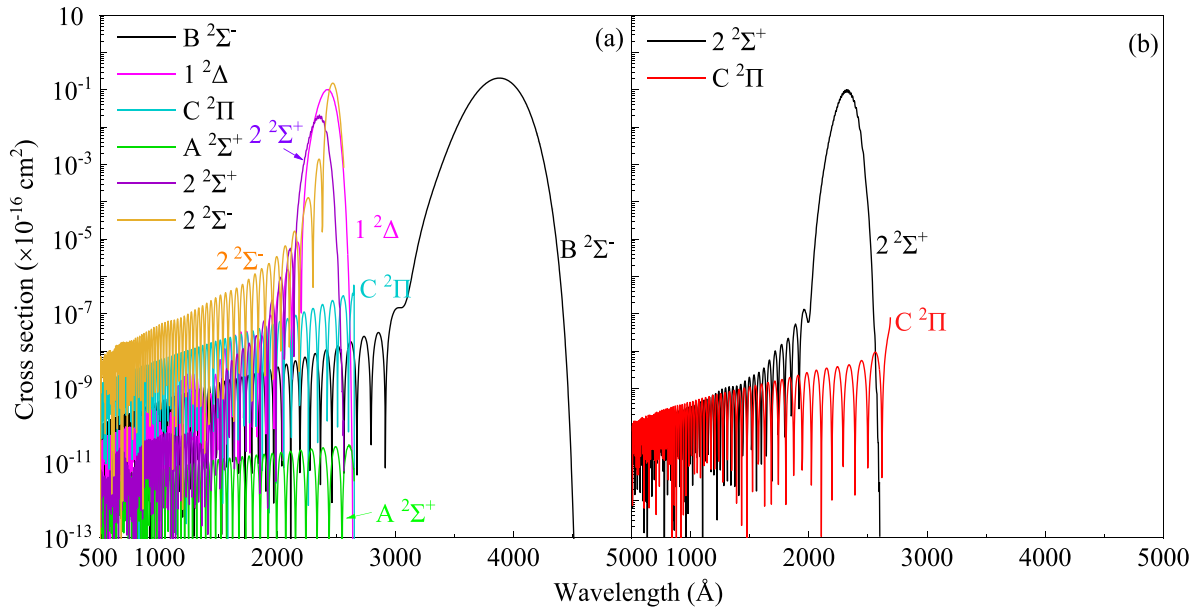
Figure 3. The state-resolved cross sections of NaO for the transitions from the rovibrational level $\upsilon'' = 0$, $N'' = 0$ of the (a) X $^2\Pi$ and (b) A $^2\Sigma^+$ states.

3.2 State-resolved cross section

The A $^2\Sigma^+$ state of NaO exhibits low quenching efficiency and has a radiative lifetime of more than 10 ms (Mitev et al. 2022). Consequently, the dissociation of a mixture of the X $^2\Pi$ and A $^2\Sigma^+$ states is requested to describe the photodissociation of NaO. The state-resolved cross sections of NaO were computed for the transitions from all rovibrational levels of the ground and first excited states to other excited states, where the X $^2\Pi$ and A $^2\Sigma^+$ states were found to support 81 and 175 vibrational levels with the maximum rotational level $N'' = 258$ and 382, respectively. Fig. 3 shows the cross sections for the transitions from rovibrational level $\upsilon'' = 0$, $N = 0$ of the X $^2\Pi$ and A $^2\Sigma^+$ states. The results show that NaO can undergo direct dissociation through the X $^2\Pi \rightarrow 1\,^2\Delta$, X $^2\Pi \rightarrow 2\,^2\Sigma^+$, X $^2\Pi \rightarrow 2\,^2\Sigma^-$, and A $^2\Sigma^+ \rightarrow 2\,^2\Sigma^+$ transitions in the far ultraviolet, as well as the X $^2\Pi \rightarrow$ B $^2\Sigma^-$ transition in the ultraviolet. This is attributed to the relatively flat PECs and weak binding of the excited states, as shown in Fig. 2(a). In contrast, the A $^2\Sigma^+$ and C $^2\Pi$ states have deep potential wells, leading to predominantly bound-bound transitions rather than bound-free transitions. As a result, these transitions exhibit very weak photodissociation cross sections.

The state-resolved cross sections for the X $^2\Pi \rightarrow 1\,^2\Delta$, X $^2\Pi \rightarrow 2\,^2\Sigma^-$, X $^2\Pi \rightarrow 2\,^2\Sigma^+$, and A $^2\Sigma^+ \rightarrow 2\,^2\Sigma^+$ transitions exhibit relatively large cross sections in the wavelength range of about 2400–2580 Å, where the cross sections for the X $^2\Pi \rightarrow 1\,^2\Delta$ transition from different rovibrational levels are highlighted in Fig. 4. As the rovibrational levels increase, the cross sections shift towards longer wavelengths. Similar trends have been observed in the photodissociation processes of other molecules (Yang et al. 2020; Bai et al. 2021).

3.3 Temperature-dependent cross section

Experimental studies of molecular photodissociation are challenging. To our knowledge, only the absolute photolysis cross sections of NaO in the wavelength range of 1930–4230 Å at temperatures of 200 and 300 K were measured by Self and Plane (2001). We calculated the cross sections at 200 and 300 K for comparison. Fig. 5 shows that our calculated cross sections are close to the measured values within the wavelength ranges of about 2400–2580 Å and 3534–4230 Å. This results also indicate the X $^2\Pi \rightarrow 1\,^2\Delta$ and X $^2\Pi \rightarrow 2\,^2\Sigma^-$ transitions in the wavelength range of about 2400–2580 Å, as well as the X $^2\Pi \rightarrow$ B $^2\Sigma^-$ transition in wavelength the range of about 3534–4230 Å, may serve as the main pathways for the photodissociation process of NaO at the temperatures of 200 and 300 K.

There is an interesting aspect that experimental cross sections exhibit a peak at approximately 3130 Å, but our calculated results show the absence of direct photodissociation processes around this wavelength. *Ab initio* calculations show that the electronic excitation energy of the C $^2\Pi$ state is accessible at about 25 000 cm^{-1} (4000 Å), and the equilibrium bond distance of the C $^2\Pi$ state is approximately 1.5 Å larger than that of the X $^2\Pi$ state. The theory predicts that the X $^2\Pi$ state may undergo transitions to high rovibrational levels of the C $^2\Pi$ state, leading to producing the absorption cross sections. However, the calculation for the absorption line intensity of the X $^2\Pi \rightarrow$ C $^2\Pi$ transition at 200 K shows that the peak position is found to be at approximately 3714 Å, as shown in Fig. 6. We guess that the PEC of the C $^2\Pi$ state may intersect with this of a higher-lying $^2\Pi$ state of NaO or interact with other electronic states through spin-orbit couplings, resulting in a pre-dissociation process. Furthermore, the X $^2\Pi$ and C $^2\Pi$ states are of the same symmetry and their adiabatic potential curves exhibit an avoided crossing at approximately 4.3 Å, as depicted in Fig. 2(a). Consequently, there would be a non-adiabatic coupling between the X $^2\Pi$ and C $^2\Pi$ states. Dynamically, this would give rise to quasi-bound states on the potential of the C $^2\Pi$ state, which could then transition into the continuum of the X $^2\Pi$ state. These resonant continuum cross sections would occur in the energy region corresponding to wavelengths of 2600–3500 Å, which is just missing part in our computed cross sections relative to experimental one (Self & Plane 2001). Note that previous studies (Gustafsson
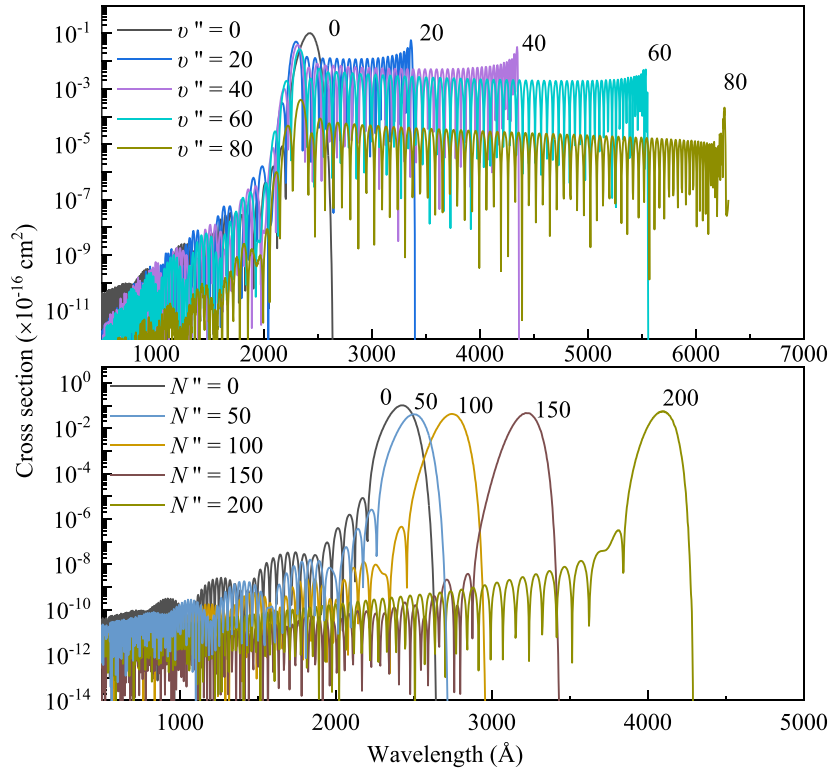
Figure 4. The state-resolved cross sections as a function of wavelength for the X $^2\Pi \to$ 1 $^2\Delta$ transition from the (a) rotational level $N'' = 0$ with different υ'' and (b) vibrational level $\upsilon'' = 0$ with different N''.
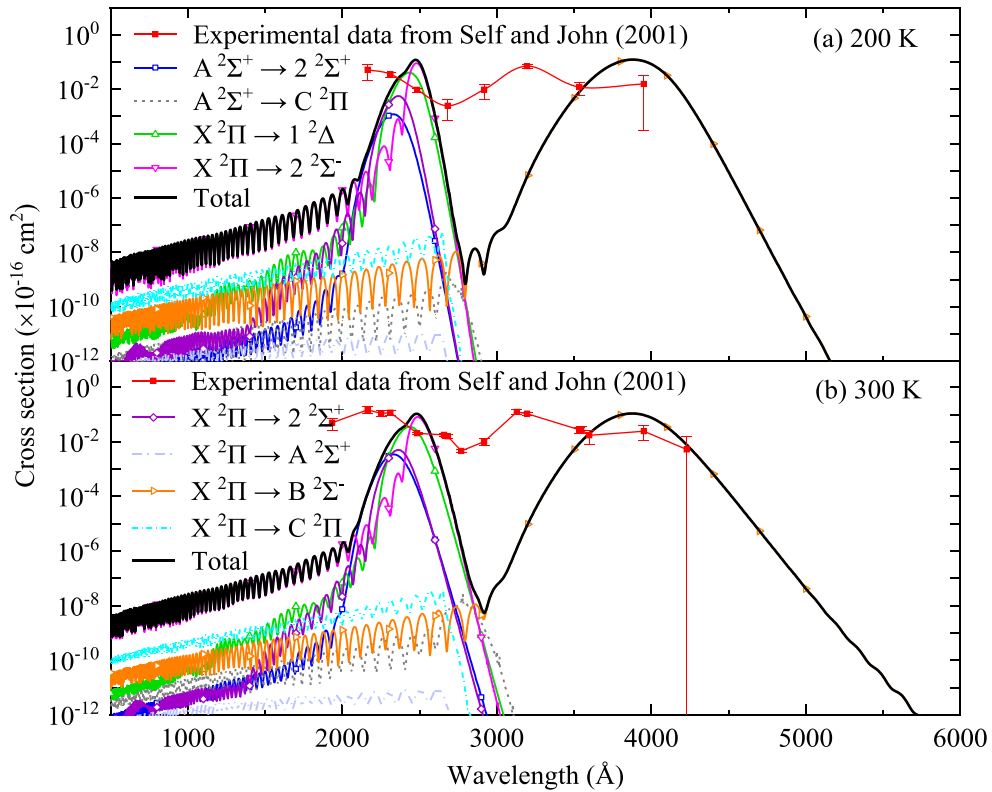

Figure 5. The cross sections of NaO at (a) 200 and (b) 300 K. The cross sections measured by Self and Plane (2001) are plotted for comparison.
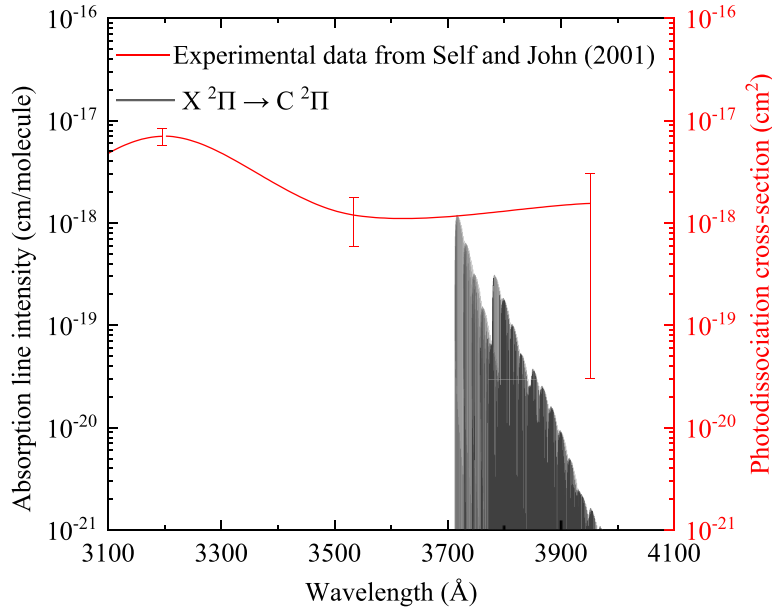
Figure 6. The absorption line intensity of the X $^2\Pi \to$ C $^2\Pi$ transition of NaO at 200 K.

2020) demonstrated the significant impact of non-adiabatic couplings on the radiative association cross section in a sodium-containing system, namely NaCl. Therefore, further theoretical investigations are warranted to delve into this problem.

Cross sections of NaO at 0, 500, 3000, and 10 000 K are presented in Fig. 7, where the cross sections for a temperature of 0 K means the state-resolved cross sections for the rovibrational level $\upsilon'' = 0, N'' = 0$. The cross sections of the X $^2\Pi \to$ A $^2\Sigma^+$ transition at the considered temperatures are below 10^{-26} cm^2 and not presented here. The cross sections exhibit distinct positive temperature dependencies at longer wavelengths. However, it is notable that the cross section at the peak generally exhibits a decrease. At low temperatures, the photodissociation processes from the X $^2\Pi$ state are highly significant, particularly the X $^2\Pi \to$ B $^2\Sigma^-$ transition dominating in the long-wavelength range. The photodissociation processes from the A $^2\Sigma^+$ state contribute less to molecular dissociation. Particularly at 0 K, the A $^2\Sigma^+$ state is entirely unpopulated according to the statistical mechanics, resulting in zero cross sections for these processes. However, as the temperature rises, the A $^2\Sigma^+ \to$ 2 $^2\Sigma^+$ and A $^2\Sigma^+ \to$ C $^2\Pi$ photodissociation processes gradually become important.

3.4 Photodissociation rates

Photochemistry modelling requires accurate knowledge of photodissociation rates. In this study, photodissociation rates of NaO in the interstellar, solar, and blackbody radiation fields were calculated for 3001 temperature points from 0 to 15 000 K. For the interstellar, solar and blackbody radiation fields, the wavelength ranges considered for the NaO dissociation were 91.2–2000, 67.1–2400, and 50–5000 nm, respectively. Fig. 8 exhibits the photodissociation rates for different electronic transitions of NaO in the interstellar and solar radiation fields.

Table 3 presents the photodissociation rates for each transition in the ISRF. The total photodissociation rates of NaO in the ISRF exhibit an approximately twofold increase as the temperature rises from 100 to 15 000 K. At low temperatures, the dominant photodissociation process occurs from the ground state to the B $^2\Sigma^-$ state. With the temperature increasing, the photolysis through the A $^2\Sigma^+ \to$ 2 $^2\Sigma^+$ transition becomes dominant. However, in comparison to the rates of HCl and HF under the radiation fields of the Sun and cooler stars, the rates of NaO in the ISRF are almost insensitive to the temperature of the molecule (Pezzella et al. 2022; Qin et al. 2022b). Similar trends can be observed in the solar radiation field.

Considering the dissociation processes of NaO in the wavelength range of 190–400 nm, Self and Plane (2001) calculated the photodissociation rates of NaO in the solar radiation field using the experimental cross sections, and they obtained the rates of 0.055 ± 0.029 and 0.093 ± 0.038 s^{-1} at 200 and 300 K, respectively. However, our calculated rates are 2.70×10^{-6} and 2.63×10^{-6} s^{-1}, which are smaller than those reported by Self and Plane (2001). These discrepancies might be attributed to the fact that our calculations only considered the direct photodissociation cross sections to calculate the rates and did not account for the cross sections associated with other processes.

Three blackbodies with temperatures of 4000, 10 000, and 20 000 K were considered to describe different types of stars. The blackbody with the temperature of $T_{rad} = 4000$ K was chosen to model T Tauri stars and stars in their early stages of formation (Appenzeller & Mundt 1989; Natta 1993). The blackbody with the temperature of $T_{rad} = 10 000$ K was used to represent the Herbig Ae stars and young A stars that are still surrounded by gas and dust envelopes (Vioque et al. 2018). The blackbody with the temperature of $T_{rad} = 20 000$ K was employed to simulate the bright and short-living B stars (Habets & Heintze 1981). Fig. 9 illustrates the temperature dependence of the photodissociation rates of NaO in these three blackbody radiation fields. It can be observed that the rates in the 4000 K black-body field increase by a factor of 4.94 from 100 to 15 000 K. However, the rates in the 10 000 and 20 000 K black-body fields do not show a significant change. Namely,
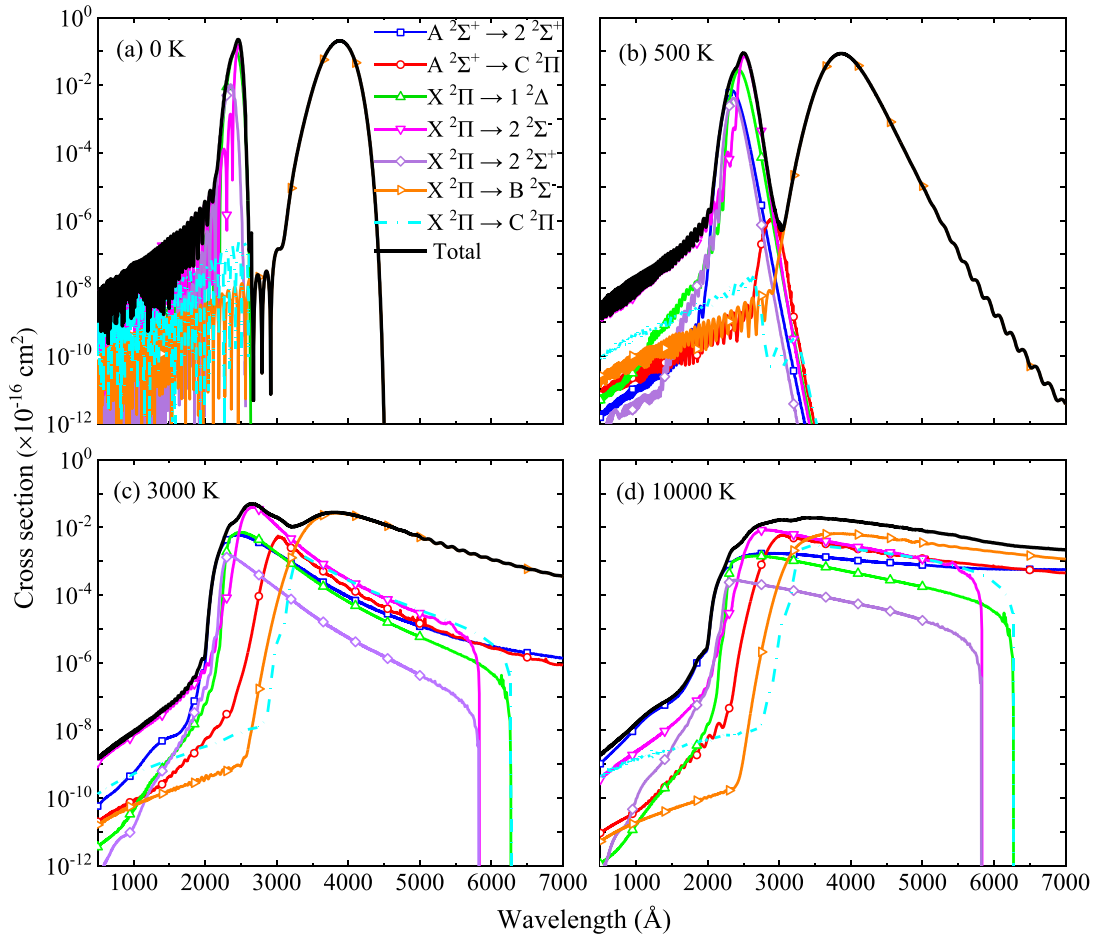
Figure 7. Photodissociation cross sections of NaO at 0, 500, 3000, and 10 000 K.
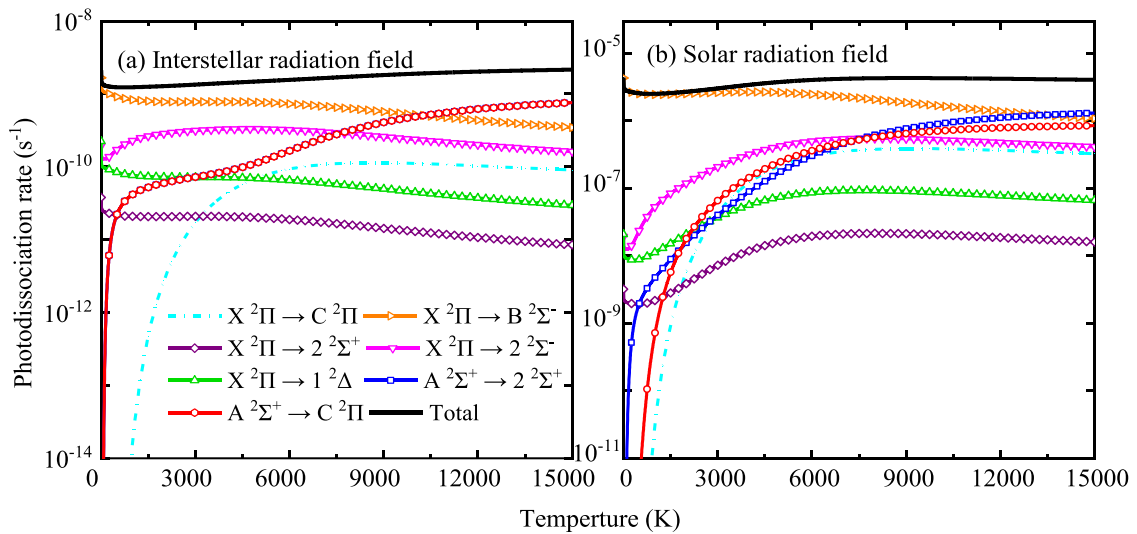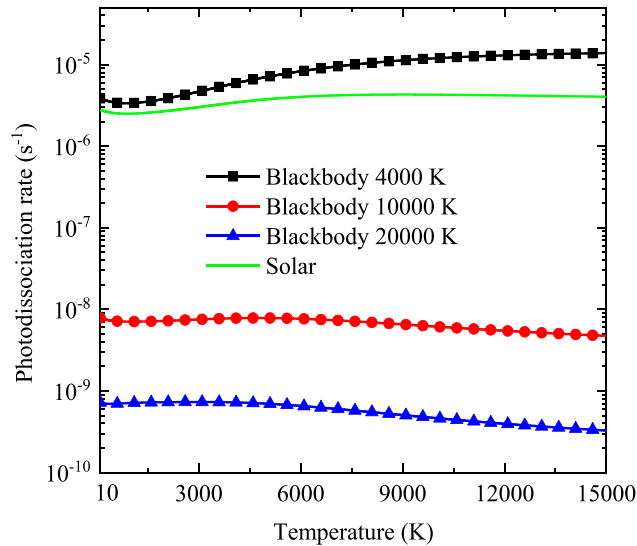
Figure 8. The photodissociation rates of NaO in the (a) interstellar and (b) solar radiation fields.

Table 3 Photodissociation rates (s^{-1}) of NaO under the standard ISRF at several temperatures.

Transition	100 K	500 K	1000 K	3000 K	5000 K	8000 K	15 000 K
$X\,^2\Pi \rightarrow C\,^2\Pi$	2.38×10^{-16}	1.52×10^{-16}	1.64×10^{-14}	1.71×10^{-11}	7.13×10^{-11}	1.12×10^{-10}	9.00×10^{-11}
$X\,^2\Pi \rightarrow B\,^2\Sigma^-$	1.06×10^{-9}	9.12×10^{-10}	8.26×10^{-10}	7.75×10^{-10}	7.64×10^{-10}	6.24×10^{-10}	3.46×10^{-10}
$X\,^2\Pi \rightarrow 2\,^2\Sigma^+$	2.41×10^{-11}	2.17×10^{-11}	2.08×10^{-11}	2.08×10^{-11}	2.01×10^{-11}	1.58×10^{-11}	8.49×10^{-12}
$X\,^2\Pi \rightarrow 2\,^2\Sigma^-$	1.27×10^{-10}	1.71×10^{-10}	2.28×10^{-10}	3.12×10^{-10}	1.62×10^{-10}	2.80×10^{-10}	1.61×10^{-10}
$X\,^2\Pi \rightarrow 1\,^2\Delta$	9.66×10^{-11}	8.40×10^{-11}	7.64×10^{-11}	7.18×10^{-11}	6.92×10^{-11}	5.48×10^{-11}	2.96×10^{-11}
$X\,^2\Pi \rightarrow A\,^2\Sigma^+$	1.39×10^{-19}	1.09×10^{-19}	1.40×10^{-19}	6.35×10^{-19}	2.67×10^{-18}	5.51×10^{-18}	5.52×10^{-18}
$A\,^2\Sigma^+ \rightarrow 2\,^2\Sigma^+$	8.66×10^{-14}	2.20×10^{-11}	4.16×10^{-11}	7.22×10^{-11}	1.15×10^{-10}	3.21×10^{-10}	7.59×10^{-10}
$A\,^2\Sigma^+ \rightarrow C\,^2\Pi$	1.12×10^{-19}	4.02×10^{-15}	6.50×10^{-13}	4.21×10^{-11}	1.15×10^{-10}	2.13×10^{-10}	2.98×10^{-10}
Total	1.31×10^{-9}	1.21×10^{-9}	1.19×10^{-9}	1.31×10^{-9}	1.48×10^{-9}	1.62×10^{-9}	1.69×10^{-9}

Figure 9. Photodissociation rates of NaO between 100 and 15 000 K for the blackbody radiation fields of 4000 K (in square), 10 000 K (in circle), and 20 000 K (in triangle).

the photodissociation rates in ultraviolet-rich radiation fields are almost insensitive to the temperature of the molecule. Furthermore, the rates in the 4000 K black-body field are larger than those in the 10 000 and 20 000 K black-body fields by approximately three to four orders of magnitude. Due to the higher intensity of the 4000 K black-body field compared to this of the solar field between 400 and 2000 nm, as shown Fig. 1, the rates in the 4000 K black-body field exceed those in the solar field by approximately 1.5–3 times.

4. CONCLUSIONS

In this work, we have calculated the cross sections and rates for the direct photodissociation of NaO. Our calculations involve transitions from the ground and first excited states to the $A\,^2\Sigma^+$, $C\,^2\Pi$, $B\,^2\Sigma^-$, $1\,^2\Delta$, $2\,^2\Sigma^+$, and $2\,^2\Sigma^-$ states using *ab initio* PECs and TDMs. The state-resolved cross sections were computed for the transitions from all rovibrational levels of the ground and first excited states. By assuming a Boltzmann distribution of rovibrational levels, the temperature-dependent cross sections were calculated at the temperature ranging from 0 to 15 000 K. The results show that the cross sections exhibit marked positive temperature dependencies at longer wavelengths. In comparison to the experiments, the $X\,^2\Pi \rightarrow 1\,^2\Delta$ and $X\,^2\Pi \rightarrow 2\,^2\Sigma^-$ transitions in the wavelength range of about 2400–2580 Å, as well as the $X\,^2\Pi$–$B\,^2\Sigma^-$ transition in the wavelength range of about 3534–4230 Å, may be the main pathways at the temperatures of 200 and 300 K.

The photodissociation rates in the interstellar, solar and blackbody radiation fields were also computed using the temperature-dependent cross sections. In the interstellar and solar radiation fields, the photodissociation process from the ground state to the $B\,^2\Sigma^-$ state dominates at low temperatures, whereas the photolysis through the $A\,^2\Sigma^+ \rightarrow 2\,^2\Sigma^+$ transition becomes dominant at high temperatures. The total rates in the interstellar, solar and high-temperature black-body radiation fields are almost insensitive to the temperature of the molecule.

DATA AVAILABILITY

All data underlying this article are available in the article and its online supplementary material. The supplementary material includes the PECs of seven electronic states, TDMs for eight transitions, temperature-dependent cross sections at individual temperatures, the rate coefficients in the interstellar, solar, and blackbody radiation fields.

The computed photodissociation cross sections are available from the ExoMol website, www.exomol.com. A new data structure about the photodissociation cross section has been constructed in the ExoMol data model (Tennyson et al. 2023).

REFERENCES

Appenzeller I., Mundt R., 1989, A&AR, 1, 291
Babb J., Smyth R. T., Mclaughlin B. M., 2019, ApJ, 876, 38
Bai T., Qin Z., Liu L., 2021, MNRAS, 505, 2177
Bai T., Qin Z., Liu L., 2023, JQSRT, 302, 108587
Berezhnoy A. A., 2013, Icarus, 226, 205
Berezhnoy A. A., 2018, Icarus, 300, 210
Brown M. E., Hill R. E., 1996, Nature, 380, 229
Chang T. Y., 1967, Rev. Mod. Phys., 39, 911
Gustafsson M., 2020, J. Chem. Phys., 153, 114305
Habets G. M. H. J., Heintze J. R. W., 1981, Astron. Astrophys. Sup., 46, 193
Hanson R. K., Spearrin R. M., Goldenstein C. S., 2016, Springer International Publishing, Switzerland
Heays A. N., Bosman A. D., Van Dishoeck E. F., 2017, A&A, 602, A105
Hugthes D. W., 1978, Wiley Interscience, New York
Hunten D., Sprague A., 1997, Adv. Space Res., 19, 1551
Johnson B. R., 1977, J. Chem. Phys., 67, 4086
Johnson B. R., 1978, J. Chem. Phys., 69, 4678
Joo S., Worsnop D. R., Kolb C. E., Kim S. K., Herschbach D. R., 1999, J. Phys. Chem. A, 103, 3193
Kirby K. P., Dishoeck E. F. V., 1989, Adv. Atom. Mol. Phys., 25, 437
Kovács I., 1969, Institute of Physics Publishing, Bristol
Kramida A., Ralchenko Y., Reader J., NIST ASD Team, 2022, NIST Atomic Spectra Database (version 5.10). Avaliable at: https://physics.nist.gov/asd, last accessed date: 2023-6-1
Langhoff S. R., Partridge H., Bauschlicher C. W., 1991, Chem. Phys., 153, 1
London F., 1937, Trans. Faraday Soc., 33, 8
McClintock W. E., Lankton M. R., 2007, Space Sci. Rev., 131, 481
Magnier S., Aubert-Frécon M., 2002, JQSRT, 75, 121
Medved M., Fowler P. W., Hutson J. M., 2000, Mol. Phys., 98, 453
Mendillo M., Laurent S., Wilson J., Baumgardner J., Konrad W. C., 2007, Nature, 448, 330
Mitev G., Taylor S., Tennyson J., Yurchenko S., Buchachenko A., Stolyarov A., 2022, MNRAS, 511, 2349
Moses J. I., Zolotov M. Y., Fegley B., Jr, 2002, Icarus, 156, 107
Natta A., 1993, ApJ, 412, 761
Pattillo R. J., Cieszewski R., Stancil P. C., Forrey R. C., Babb J. F., McCann J. F., McLaughlin B. M., 2018, ApJ, 858, 10
Pezzella M., Tennyson J., Yurchenko S. N., 2022, MNRAS, 514, 4413
Plane J., 2004, Atmos. Chem. Phys., 4, 627
Plane J. M. C., 1991, Int. Rev. Phys. Chem., 10, 55
Potter A., Morgan T., 1988, Science, 241, 675
Qin Z., Bai T., Liu L., 2021, ApJ, 917, 87
Qin Z., Bai T., Liu L., 2022a, MNRAS, 510, 3011
Qin Z., Bai T., Liu L., 2022b, MNRAS, 516, 550
Sarantos M., Killen R. M., Sharma A. S., Slavin J. A., 2010, Icarus, 205, 364
Self D. E., Plane J. M. C., 2001, Phys. Chem. Chem. Phys., 4, 16
Semenov M., El-Kork N., Yurchenko S. N., Tennyson J., 2021, Phys. Chem. Chem. Phys., 23, 22057
Smith S., Wilson J., Baumgardner J., Mendillo M., 1999, Geophys. Res. Lett., 26, 1649
Soldán P., Lee E. P., Gamblin S. D., Wright T. G., 1999, Phys. Chem. Chem. Phys., 1, 4947
Sprague A., Sarantos M., Hunten D., Hill R., Kozlowski R., 2012, Can. J. Phys., 90, 725
Tennyson J., Pezzella M., Zhang J., Yurchenko S. N., 2023, RASTAI, 2, 231
Valiev R. R., Berezhnoy A. A., Sidorenko A. D., Merzlikin B. S., Cherepanov V. N., 2017, Planet. Space Sci., 145, 38
Valiev R. R., Berezhnoy A. A., Gritsenko I. S., Merzlikin B. S., Cherepanov V. N., T. K., Whler C., 2020, A&A, 633, A39
Vioque M., Oudmaijer R., Baines D., Mendigutía I., Pérez-Martínez R., 2018, A&A, 620, A128
Werner H.-J. et al., 2015, Molpro (Version 2015.1), A Package of Ab Initio Programs. Available at: http://www.molpro.net/, last accessed date: 2023-2-1
Xu J., Smith A., 2005, J. Atmos. Sol-Terr. Phys., 67, 1216
Yakshinskiy B., Madey T., 1999, Nature, 400, 642
Yamada C., Fujitake M., Hirota E., 1989, J. Chem. Phys., 90, 3033
Yang Y. K., Cheng Y., Peng Y. G., Wu Y., Wang J. G., Qu Y. Z., Zhang S. B., 2020, JQSRT, 254, 107203

SUPPORTING INFORMATION

Supplementary data are available at *MNRAS* online.

Please note: Oxford University Press is not responsible for the content or functionality of any supporting materials supplied by the authors. Any queries (other than missing material) should be directed to the corresponding authors for the article.

This paper has been typeset from a TₑX/LATₑX file prepared by the author.